
This is the **submitted version** of the journal article:

Li, Junshan; Wang, Xiang; Xing, Congcong; [et al.]. «Electrochemical reforming of ethanol with acetate Co-Production on nickel cobalt selenide nanoparticles». Chemical engineering journal, Vol. 440 (Jul.2022), art. 135817. DOI 10.1016/j.cej.2022.135817

This version is available at <https://ddd.uab.cat/record/270833>

under the terms of the  license

Electrochemical Reforming of Ethanol with Acetate Co-Production on Nickel Cobalt Selenide Nanoparticles

Junshan Li,^{ab} Xiang Wang,^c Congcong Xing,^c Luming Li,^a Shijia Mu,^b Xu Han,^d Ren He,^c Zhifu Liang,^{c,d} Paulina Martinez,^c Yunan Yi,^b Qianbao Wu,^b Huiyan Pan,^c Jordi Arbiol,^{d,f} Chunhua Cui,^{b*} Yu Zhang,^{c*} Andreu Cabot^{c,f*}

a Institute of Advanced Study, Chengdu University, 610106, Chengdu, China

b Institute of Fundamental and Frontier Sciences, University of Electronic Science and Technology of China, 610054, Chengdu, China.

c Catalonia Institute for Energy Research - IREC, Sant Adrià de Besòs, 08930, Barcelona, Catalonia, Spain.

d Catalan Institute of Nanoscience and Nanotechnology (ICN2), CSIC and BIST, Campus UAB, Bellaterra, 08193, Barcelona, Catalonia, Spain.

e School of Biological and Chemical Engineering, Nanyang Institute of Science and Technology, Nanyang, 473004, China

f ICREA, Pg. Lluís Companys 23, 08010, Barcelona, Catalonia, Spain.

Abstract: The energy efficiency of water electrolysis is limited by the sluggish reaction kinetics of the anodic oxygen evolution reaction (OER). To overcome this limitation, OER can be replaced by a less demanding oxidation reaction, which in the ideal scenario could be even used to generate additional valuable chemicals. Herein, we focus on the electrochemical reforming of ethanol in alkaline media to generate hydrogen at a Pt cathode and acetate as a co-product at a $\text{Ni}_{1-x}\text{Co}_x\text{Se}_2$ anode. We first detail the solution synthesis of a series of $\text{Ni}_{1-x}\text{Co}_x\text{Se}_2$ electrocatalysts. By adjusting the Ni/Co ratio, the electrocatalytic activity and selectivity for the production of acetate from ethanol are optimized. Best performances are obtained at low substitutions of Ni by Co in the cubic NiSe_2 phase. Density function theory reveals that the Co substitution can effectively enhance the ethanol adsorption and decrease the energy barrier for its first step dehydrogenation during its conversion to acetate. However, we experimentally observe that too large amounts of Co decrease the Faradaic efficiency from values

27 above 90% to just 50 %. At the optimized composition, the $\text{Ni}_{0.75}\text{Co}_{0.25}\text{Se}_2$ electrode delivers a stable
28 chronoamperometry current density of up to 45 mA cm^{-2} , corresponding to 1.2 A g^{-1} , in a 1 M KOH +
29 1 M ethanol solution, with a high Faradaic efficiency of 82.2% at a relatively low potential, 1.50 V vs.
30 RHE, and with an acetate production rate of $0.34 \text{ mmol cm}^{-2} \text{ h}^{-1}$.

31 **Keywords:** Electrocatalysis; ethanol reforming; hydrogen production; selenide nanoparticle; acetate.

32

33

34

1. Introduction

Molecular hydrogen is a convenient carbon-free energy carrier and a key component in the chemical industry. While molecular hydrogen does not exist in nature, it can be produced by water electrolysis using renewable energy sources such as wind, hydropower, and solar.[1] However, while water electrolysis systems have been commercialized for several years, their high cost has prevented extensive deployment, and most molecular hydrogen is still being produced by the partial oxidation and steam reforming of natural gas and coal gasification.[2] To turn this trend around, cost-effective strategies for the production of hydrogen from renewable sources need to be developed. In this context, biomass-derived products provide an excellent alternative source of hydrogen owing to their renewable character and their net-zero CO₂ footprint.[3] Besides, the partial oxidation of an organic molecule offers a less energy demanding anodic oxidation reaction, which can contribute to overcoming the energy efficiency limitation of water electrolysis associated with the sluggish reaction kinetics of the oxygen evolution reaction (OER).[4] An additional advantage of the production of hydrogen from the reforming of waste or biomass-derived organics is the potential co-generation of valuable organic chemicals, which can both improve process economics and further diminish the dependence on fossil resources that are currently used to produce them.[5–7] On top of these advantages, the replacement of OER by an organic oxidation reaction enables the implementation of coupled cost-effective waste abatement processes. Thus, overall, the clean electrochemical conversion of organic waste and biomass-derived products into value-added chemicals driven by renewable energy has both high fundamental interest and enormous potential for socio-economic and environmental impact.[8–11]

In this scenario, (bio)ethanol is a paradigmatic and particularly interesting hydrogen source. Ethanol is

a key commodity in the chemical industry, used as a precursor or building block for the synthesis of a plethora of chemicals, including formaldehyde, acetic acid, and plastics.[12,13] Ethanol can be renewably generated from the reduction of CO₂ and several biomass-derived feedstocks and organic residues such as sewage sludge.[12-14] As a liquid, ethanol can be easily stored and transported. Besides, bioethanol aqueous solutions can be directly used in electrocatalytic processes, without the need for purification. Compared with water splitting, the production of hydrogen from ethanol is thermodynamically advantageous ($\Delta G^0 = +237 \text{ kJ}\cdot\text{mol}^{-1}$ for water oxidation vs. $\Delta G^0 = +9.6 \text{ kJ}\cdot\text{mol}^{-1}$ for ethanol oxidation to acetate), which decreases the energy input required.[14] The reforming of ethanol also prevents the H₂ and O₂ back reaction. Besides, compared with the complete ethanol reforming down to CO₂, the production of H₂ and acetate could have higher economical profitability associated with the high economic value of acetate as a side product.[15]

In terms of catalysts, while OER generally requires high-cost noble metal electrocatalysts, the electrooxidation of organic molecules, such as methanol or ethanol, in alkaline media can be activated at lower cost using abundant noble-metal-free transition metal electrocatalysts, e.g. nickel, iron and cobalt.[12,16,17] Among them, nickel chalcogenides have demonstrated particularly high activity and selectivity for the conversion of methanol to formate,[18–23] thus we hypothesize them to be excellent ethanol oxidation catalysts.

Herein, we detail the preparation of bimetallic Ni-Co selenides nanoparticles (NPs) over a full range of compositions using a solution-based strategy. This set of materials is tested for the partial electrooxidation of ethanol in an alkaline electrolyte. Finally, the material is optimized to minimize the overpotential and maximize the activity and Faradaic efficiency for ethanol to acetate conversion.

2. Experimental section

2.1. Chemicals

All chemicals, including cobalt(II) acetylacetonate ($\text{Co}(\text{acac})_2$, 97%, Sigma Aldrich), selenium powder (Se, 200 mesh, 99.5%, Acros Organics), nickel(II) acetylacetonate ($\text{Ni}(\text{acac})_2$, 96%), oleylamine (OAm, $\text{C}_{18}\text{H}_{37}\text{N}$, 80-90%, Acros Organics), potassium hydroxide (KOH, 85%, Sigma Aldrich), potassium carbonate (K_2CO_3 , 99.5%, Sigma Aldrich), potassium bicarbonate (KHCO_3 , 99.7%, Sigma Aldrich), 1,2-ethanedithiol (EDT, $\text{HSCH}_2\text{CH}_2\text{SH}$, 98%, Sigma Aldrich), oleic acid (OAc, $\text{C}_{18}\text{H}_{34}\text{O}_2$, 99%, Sigma Aldrich), carbon black (CB, Vulcan XC72, Sigma Aldrich), and Nafion (10 wt.%, perfluorinated ion-exchange resin, dispersion in water, Sigma Aldrich), were used as received, without further treatment. Analytical grade chloroform and ethanol for the washing process were obtained from various sources. MilliQ water ($18.2 \text{ M}\Omega\cdot\text{cm}$) was used for electrolyte and ink preparation, and ion chromatography (IC) measurements. An argon-filled glove box was used to handle sensitive chemicals and for ink preparation.

2.2. Solution-based synthesis of $\text{Ni}_{1-x}\text{Co}_x\text{Se}_2$ NPs

Bimetallic selenide NPs were produced from a two-step process involving the preparation of a reactive ink and its decomposition. First, the precursor ink was prepared inside an argon-filled glove box by dissolving $(1-x)$ mM of $\text{Ni}(\text{acac})_2$, x mM of $\text{Co}(\text{acac})_2$, and 8 mM of Se powder inside a vial with 30 mL of OAm and 3 mL of EDT under vigorous stirring for 1h at 50 °C. The obtained solution was then filtered through a 0.2 μm filter. Then, 36 mL of the prepared precursor together with 60 mL of OAm and 30 mL OAc were placed in a 250 mL three-neck flask and vacuumed at 60 °C for 30 min followed by heating to 220 °C under Ar at a rate of 5°C/min. After reacting for 20 min, the solution was rapidly cooled down to room temperature in a water bath. Next, the crude solution was mixed with 60 mL of

chloroform and then centrifuged at 8000 rpm for 5 min. The washing process was repeated by dispersion in chloroform/ethanol and centrifugation several times. Finally, the obtained product was stored in chloroform and stored in the glovebox.

2.3. Material characterization

Laboratory X-ray diffraction (XRD) was performed on a Bruker AXS D8 Advance (Cu K radiation: $\lambda = 1.5106 \text{ \AA}$) to study the crystal structure. Scanning electron microscopy (SEM) with energy dispersive spectroscopy (EDS) measurements were conducted on a Gemini 300 field emission scanning electron microscope (Zeiss, Germany) equipped with an AZtecOne UltimMax40 energy spectrometer. High-resolution transition electron microscopy (HRTEM) and scanning TEM (STEM) investigation were performed on a field emission gun FEI Tecnai F20 microscope. High angle annular dark-field (HAADF) STEM was combined with electron energy loss spectroscopy (EELS) in the Tecnai microscope using a Gatan Quantum filter. X-ray photoelectron spectroscopy (XPS) analyses were conducted on a Specs system.

2.4. Electrochemical characterization

Electrochemical tests were carried out on a Bio-logic SP-200 potentiostat using a conventional three-electrode system including a Pt wire as the counter electrode, a Hg/HgO reference electrode, and the $\text{Ni}_{1-x}\text{Co}_x\text{Se}_2$ NPs supported on CB on top of a 5 mm diameter glassy carbon (GC) as working electrode (WE). To prepare the WE, a catalytic ink was prepared by dispersing 3 mg of dried NPs and 6 mg of CB in a vial containing 1.8 ml of MilliQ water/ethanol (v/v = 1:1) and 100 μL of a 10 wt% Nafion solution, followed by half-an-hour of vigorous sonication. Afterwards, 5 μL of this ink were drop-casted on a carefully polished GC electrode and dried naturally in air. Before the measurement, the alkaline electrolyte was bubbled with high-purity N_2 gas for half an hour. Cyclic voltammetry (CV)

and chronoamperometry (CA) were applied to study the electrocatalytic performance. To analyze the product of the oxidation reaction at the anode and calculate the faradaic efficiency, 0.5 mL of the solution was collected, diluted 20-fold with MilliQ water, and then analyzed by IC. A freshly prepared 4.5 mM KCO₃ and 0.8 mM KHCO₃ solution was used as leachate solution for the measurement. The amount of product was quantified with a standard curve obtained from known acetate concentrations. At the cathode, the generated hydrogen was determined by gas chromatography (GC, 8890, Agilent Technologies) connected to the electrocatalytic cell. Before measurement, a stable flow rate of 20 cm³ min⁻¹ Ar (99.999%) was bubbled for 30 mins at the Pt wire in an H-type two-compartment cell, which is separated by a Nafion-115 proton membrane. The GC product analysis was conducted every 12 mins. The produced gas was identified and quantified by a calibration curve using known concentrations of standard H₂ gas. All obtained potentials (vs. Hg/HgO) were converted to the reversible hydrogen electrode (RHE) reference according to the Nernst equation: $E_{RHE} = E_{Hg/HgO} + 0.059 \times \text{pH} + E^{\circ}_{Hg/HgO}$, where $E_{Hg/HgO}$ is the measured potential, $E^{\circ}_{Hg/HgO}$ is the reference potential of 0.098 V, and pH is 13.6 as it corresponds to the 1.0 M KOH solution. All current densities were referred to the geometrical area of the GC electrode, i.e. 0.196 cm².

2.5 Computational method

The Vienna ab initio package (VASP) was used to perform all the density functional theory (DFT) calculations within the generalized gradient approximation (GGA) using the PBE formulation. [24–26] The projected augmented wave (PAW) potential was used to describe the ionic cores and valence electrons were taken into account using a plane wave basis set with a kinetic energy cutoff of 400 eV.[27,28] Partial occupancies of the Kohn–Sham orbitals were allowed using the Gaussian smearing method and a width of 0.05 eV. The electronic energy was considered self-consistent when the energy

change was smaller than 10^{-5} eV. A geometry optimization was considered convergent when the force change was smaller than 0.02 eV/Å. Grimme's DFT-D3 methodology was used to describe the dispersion interactions.[29]

Using a $7 \times 11 \times 9$ Monkhorst-Pack k-point grid for Brillouin zone sampling, the equilibrium lattice constants of the monoclinic NiOOH unit cell were optimized to be $a=5.168$ Å, $b=2.847$ Å, $c=4.516$ Å, at $\alpha=90^\circ$, $\beta=107.1^\circ$, $\gamma=90^\circ$. They were used to construct a NiOOH(001) surface model (model 1) with $p(2 \times 3)$ periodicity in the x and y directions and 1 stoichiometric layer in the z direction separated by a vacuum layer in the depth of 15 Å to separate the surface slab from its periodic duplicates. In another model (model 2), three Co atoms were doped into model 1 by replacing three Ni atoms. One O atom was removed from both models to create an oxygen vacancy. During structural optimizations, the gamma point in the Brillouin zone was used for k-point sampling, and all atoms were allowed to relax.

The free energy of a gas phase molecule or an adsorbate on the surface was calculated by the equation $G = E + \text{ZPE} - TS$, where E is the total energy, ZPE is the zero-point energy, T is the temperature in kelvin (298.15 K), and S is the entropy.

3. Results and discussion

3.1. Characterization of catalysts

Ni_{1-x}Co_xSe₂ NPs were produced through a two-step process involving the preparation of a reactive ink from the dissolution of Se and the proper amount of Ni and Co precursors in EDT and OAm and its posterior reaction (see the experimental section for details and Fig. 1a). Fig. 1b displays the XRD patterns of the obtained Ni_{1-x}Co_xSe₂, with $0 \leq x \leq 1$. For $x=0$ and $x=1$, the crystal structures of NiSe₂ and CoSe₂ could be properly index with the cubic pa-3 (JCPDS No. 01 088 1771) and the orthorhombic

pnm (JCPDS No. 00 053 0449) phases, respectively. With increasing amounts of Co within the NiSe₂ structure, a continuous transition from the cubic NiSe₂ phase to the orthorhombic CoSe₂ structure was observed. Within the experimental error, SEM-EDS analyses showed the composition of the obtained materials to be consistent with the nominal Ni/Co ratios (Fig. S1). Thus, in the following, we refer to the different samples using the nominal values.

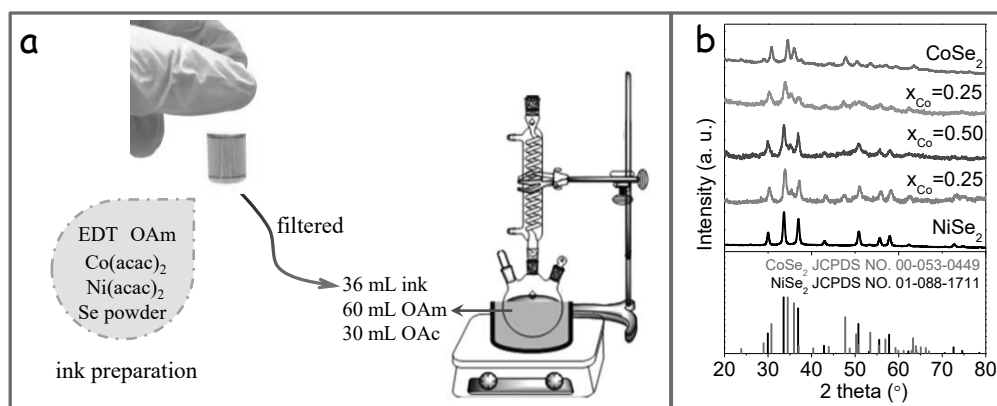


Fig. 1. (a) Schematic drawing of the solution-based process used to produce Ni_{1-x}Co_xSe₂ NPs. (b) XRD pattern of the as-synthesized product.

Fig. 2a displays a representative TEM micrograph of the Ni_{0.75}Co_{0.25}Se₂ sample. It consists of NPs having an average diameter of around 16 nm. When varying the Co composition over the entire Ni/Co range, the NPs size remained unchanged (Fig. S2). HRTEM micrographs show the NPs to be highly crystalline (Fig. 2b). The lattice parameter of the Ni_{0.75}Co_{0.25}Se₂ NPs is $a=b=c=5.840$ Å, which is in between that of the NiSe₂ cubic phase ($a=b=c=5.973$ Å) and the CoSe₂ cubic phase ($a=b=c=5.681$ Å), in good agreement with a lattice containing a mixture of both cations Ni_xCo_{1-x}Se₂. According to Vegard's law, and considering a linear approximation, the amount of Co present in the structure is estimated at $x=0.46$ for the Ni_{0.75}Co_{0.25}Se₂ sample. The composition deviation obtained from Vegard's law can be attributed to the different bonding forces of Ni and Co with selenium within the selenide.[30] As can be seen in the EELS compositional maps (Fig. 2c), the Ni_{0.75}Co_{0.25}Se₂ NPs display

a homogeneous distribution of the three elements, with an average ratio Ni/Co=7/3, consistent with the nominal composition and EDS data.

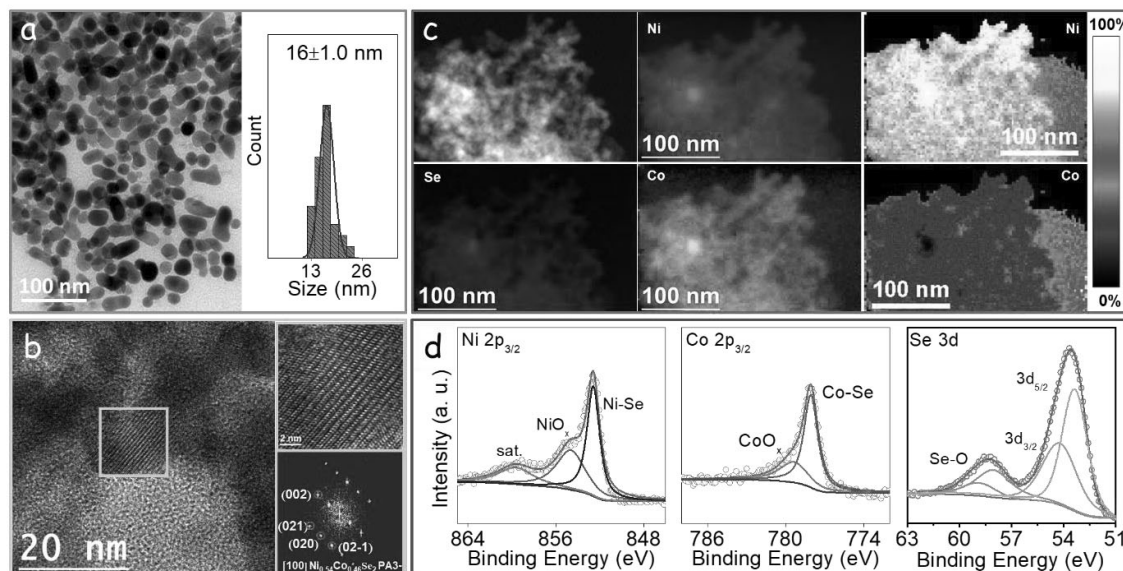


Fig. 2. TEM and XPS characterization of $\text{Ni}_{0.75}\text{Co}_{0.25}\text{Se}_2$ NPs. (a) TEM image and size distribution histogram. (b) HRTEM micrograph and indexed power spectra. (c) HAADF STEM image and EELS-STEM compositional maps obtained from HAADF STEM shown region. Individual Ni L2,3-edges at 855 eV (red), Co L2,3-edges at 779 eV (red), and Se M1-edges at 231 eV (blue) composition maps. Colour gradient maps display the relative compositions of Ni and Co. The colour scale is the same for both panels (Ni and Co). (d) Ni $2p_{3/2}$, Co $2p_{3/2}$, and Se $3d$ high resolution XPS spectra.

XPS analysis was used to characterize the surface composition and element oxidation state (Fig. 2d and Fig. S3). Figure 2d displays the high resolution Ni $2p_{3/2}$, Co $2p_{3/2}$, and Se $3d$ XPS spectra of $\text{Ni}_{0.75}\text{Co}_{0.25}\text{Se}_2$ NPs. Each of the three elements presents two chemical states that we associate with a metal selenide and a metal oxide environment, in good agreement with previous publications including an XPS characterization of nickel- and cobalt- selenides.[31,32] Specifically, aside from a satellite peak at 859.8 eV, the Ni $2p_{3/2}$ region shows the presence of two chemical states that we associate with Ni ions within Ni-Se (852.6 eV) and within Ni-O (854.7 eV) chemical environments.[33] The Co $2p_{3/2}$ region also shows two chemical environments associated with Co-Se (778.0 eV) and Co-O (779.4

eV).[34] Finally, the Se 3d XPS spectrum shows a component at 53.4 eV associated with a metal selenide environment and a component at 58.4 eV associated with a selenium oxide environment.[35] The surface oxide component was attributed to the partial oxidation of the NPs surface during XPS sample preparation and transportation.[36]

3.2. Electrocatalytic performance

Working electrodes were prepared by coating a glassy carbon with a catalyst ink prepared by mixing dried NPs and CB in an ethanol/water solution containing Nafion. The electrochemical performance was explored in a conventional three-electrode electrochemical cell using a Pt wire as the counter electrode and a Hg/HgO reference electrode (see the experimental section for details).

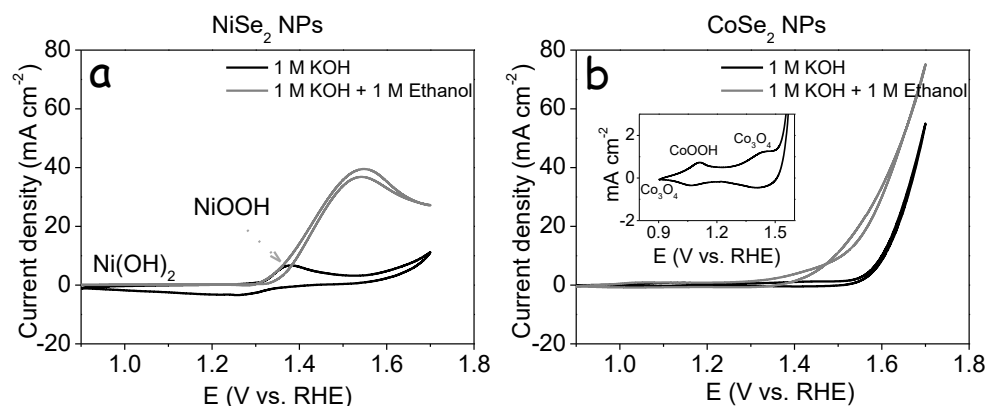


Fig. 3. Electrocatalytic performance for (a) NiSe₂ NP-based electrodes, and (b) CoSe₂ NP-based electrodes electrolyte containing a 1 M KOH (red curve) and a 1 M KOH + 1 M ethanol (black curve).

First, NiSe₂- and CoSe₂-based electrodes were tested in the potential window 0.9-1.7 V vs. RHE with a scan rate of 50 mV s⁻¹ in 1 M KOH electrolyte solution. In a basic solution, a hydroxide is formed on the surface of Ni oxides and Ni chalcogenides.[37] As shown in Fig. 3a, during the forward scan, the first current density peak measured from NiSe₂-based electrodes (black curve) was attributed to the oxidation of surface Ni(OH)₂ to NiOOH at around 1.392 V vs. RHE. At higher applied potential, above ca. 1.65 V vs RHE, a rise in the current density was associated with the OER. During the

reverse scan, NiSe₂-based electrodes displayed a NiOOH to Ni(OH)₂ reduction peak at around 1.380 V vs. RHE.

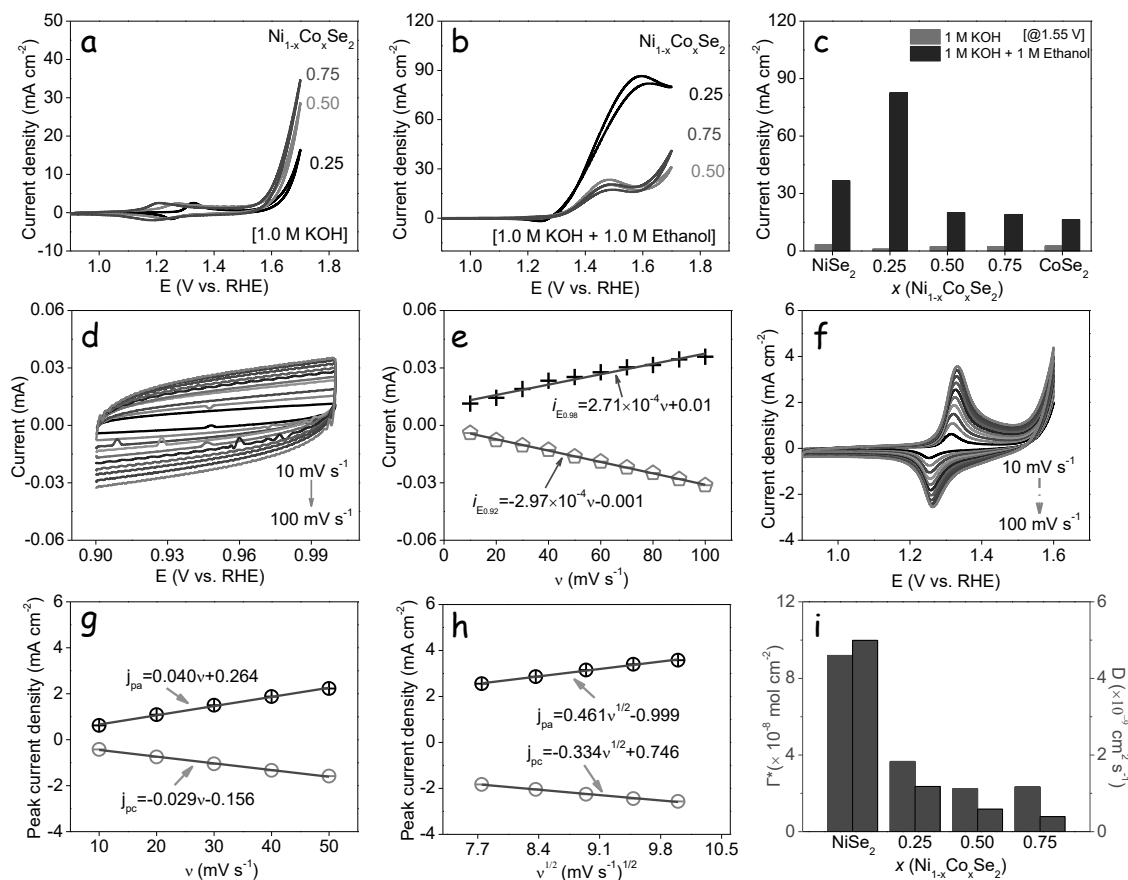


Fig. 4. (a) CV curves for the Ni_{1-x}Co_xSe₂ (x=0.25; 0.50; 0.75) electrodes in 1 M KOH electrolyte in the potential range from 0.9 V to 1.7 V with a scan rate of 50 mV s⁻¹. (b) CV curves in 1M KOH + 1M ethanol electrolyte. (c) Current densities in 1 M KOH (green) and 1M KOH + 1M ethanol electrolyte (blue) at 1.55 V vs. RHE. (d) CV curves of Ni_{1-x}Co_xSe₂ (x=0.25) based electrode in 1.0 M KOH in the non-Faradaic potential range (0.9-1.0 V) with a scan rate of 10-100 mV s⁻¹. (e) Linear fit of the forward current at 0.98 V and backward current at 0.92 V as a function of scan rate, from 10 to 100 mV s⁻¹. (f) CV curves of a Ni_{1-x}Co_xSe₂ (x=0.25) electrode in the potential range from 1.0 V to 1.60 V with a variable scan rate, from 10-100 mV s⁻¹. (g) Linear fit of the peak current and scan rate from 10 to 50 mV s⁻¹. (h) Liner fit of the peak current and square root of scan rate 60 to 100 mV s⁻¹. (i) Comparison of the surface coverage of redox species (Γ*) and diffusion coefficient (D) for the Ni-containing Ni_{1-x}Co_xSe₂ NPs based electrode in 1 M KOH solution.

For the CoSe₂-based electrode in 1M KOH solution (black curve in Fig. 3b), two small current density peaks in the forward scan were observed. In an alkaline medium, the surface of Co-based

chalcogenides is generally oxidized.[38–40] During the forward scan, the surface cobalt oxide is further oxidized probably to CoOOH at 1.11 V vs. RHE. At ca. 1.439 V vs RHE, CoOOH is even further oxidized, possibly to CoO₂. These phases are reduced during the reverse scan. At ca. 1.60 V vs. RHE, the OER is activated on the CoSe₂-based electrode, showing a significantly higher OER activity than the NiSe₂-based electrode. Upon adding 1M ethanol to the electrolyte solution, a sharp rise in the current density (red curves in Fig. 3) and corresponding to the ethanol oxidation reaction (EOR) was measured at ca. 1.35 V for both NiSe₂- and CoSe₂-based electrodes. Above the OER onset potential, both reactions, OER and EOR, compete with each other [41–43].

Figure 4 displays the results from the electrochemical characterization of the electrodes based on ternary chalcogenides, Ni_{1-x}Co_xSe₂. In a 1M KOH solution, we observed the OER activity to increase with the amount of Co. Specifically, as shown in Fig. 4a, the potential required to generate 10 mA cm⁻² decreased from 1.698 V for NiSe₂, to 1.672 V for x=0.25, 1.638 V for x=0.50, and 1.620 V for x=0.75. These values were still above that of CoSe₂ electrodes, 1.599 V (Table S1).

When adding 1M ethanol to the electrolyte, a rapid current density increase at lower potentials was observed. In contrast with the OER, the overpotential for EOR at 10 mA cm⁻² did not follow a monotonous trend with the Co introduction, but we observed the addition of a small amount of Co to result in the highest improvement of the results obtained for NiSe₂ (Fig. 4b and Table S1). Figure 4c compares the current density of the different electrodes at a fixed potential, 1.55 V, significantly below the OER onset potential. After subtracting the current density measured in 1 M KOH solution, the net EOR current density increased from 33.3 mA cm⁻² for NiSe₂, to 81.6 mA cm⁻² for Ni_{0.75}Co_{0.25}Se₂, and decreased at higher Co concentrations. If considering the loading mass of NPs, the highest mass current density at 1.55 V was also obtained for the Ni_{0.75}Co_{0.25}Se₂ electrode, 2.1 A mg⁻¹, and it was

significantly above that of recently reported Ni NPs/C,[44] Co₃O₄ nanosheets,[45] CoNi hydroxide nanosheets,[46] and fluorine-modified FeOOH,[47] and comparable to that of phosphine doped CoS₂,[48] Ni-Fe phosphide and Co₃S₄ nanosheets (Table S2).[49,50]

As shown in Fig. 4d, a double-layer pattern for Ni_{0.75}Co_{0.25}Se₂ NPs was obtained in 1 M KOH in the potential window of 0.9 V-1.0 V from 10 mV s⁻¹ to 100 mV s⁻¹. The electrochemical double-layer capacitance (*C_{dl}*) in the non-faradaic region was calculated from the linear fit of the current (*i*) with the scan rate (*v*):

$$i_c = v C_{dl}$$

From this capacitance, the electrochemical active area (ECSA) was determined using the following equation:

$$ECSA = C_{dl}/C_s$$

where *C_s* is 0.04 mF cm⁻², according to the values reported for Ni-based electrodes in alkaline solution.[51] By averaging the slope obtained from the forward scan at 0.98 V and backward scan at 0.92 V (Fig. 4e), the calculated ECSA for Ni_{0.75}Co_{0.25}Se₂ was 90.1 cm² g⁻¹, well above the values obtained for NiSe₂ (75.7 cm² g⁻¹), Ni_{0.50}Co_{0.50}Se₂ (71.0 cm² g⁻¹), and Ni_{0.25}Co_{0.75}Se₂ (49.7 cm² g⁻¹) electrodes (Fig. S4 and Table S1).

The CV curves of the bimetallic selenides displayed just one peak in the forward scan and one peak in the reverse scan (Fig. S5). The peak current density for the bimetallic selenides was found at lower potentials than for NiSe₂ (1.381 V) and the peak potential decreased with the amount of Co introduced, from 1.371 for NiSe₂ to 1.209 V for Ni_{0.25}Co_{0.75}Se₂. On the other hand, the voltage of the peak current density in the backward scan did not change monotonically with the amount of Co introduced, but it increased from NiSe₂ (1.219 V) to Ni_{0.25}Co_{0.75}Se₂ (1.249 V) and decreased at higher Co concentrations.

Associating these peaks to the $\text{Ni}(\text{OH})_2 \rightleftharpoons \text{NiOOH}$ redox reaction, we observed the potential difference ΔE_p between the oxidation and reduction peaks decreased from 162 mV for NiSe_2 to 79, 40, and 20 mV with an increasing amount of Co. The smaller potential differences are related to the improved electron transfer kinetics between the electrode surface and the active centres, associated with the modified electronic structure of the bimetallic selenides.[52]

The surface coverage of $\text{Ni}(\text{OH})_2/\text{NiOOH}$ redox species was determined from the dependence of the peak current density on the scan rate. Fig. 4h shows CV profiles from the $\text{Ni}_{0.75}\text{Co}_{0.25}\text{Se}_2$ electrode in 1 M KOH solution at 10-100 mV s^{-1} . The redox peak associated with the $\text{Ni}(\text{OH})_2 \rightleftharpoons \text{NiOOH}$ redox reaction can be observed in the positive and negative scans. From the linear relationship between the peak current density and the scan rate from 10-50 mV s^{-1} , the surface coverage of $\text{Ni}(\text{OH})_2/\text{NiOOH}$ redox species (Γ^*) was determined using the following equation:

$$I_p = \left(\frac{n^2 F^2}{4RT} \right) A \Gamma^* v$$

where n is the number of transferred electrons (assumed to be 1 for $\text{Ni}(\text{OH})_2/\text{NiOOH}$), F is the Faraday constant (96,845 C mol^{-1}), R is the gas constant (8.314 $\text{J K}^{-1} \text{mol}^{-1}$), T is the absolute temperature (295 K) and A is the geometric surface area of the GC electrode (0.196 cm^2). Γ^* was calculated considering the average of the fitted slopes for the anodic and cathodic peaks. As expected, the surface coverage of redox species, Γ^* , measured for the $\text{Ni}_{0.75}\text{Co}_{0.25}\text{Se}_2$ electrode, $3.7 \times 10^{-8} \text{ mol cm}^{-2}$, was well below that of NiSe_2 , $9.2 \times 10^{-8} \text{ mol cm}^{-2}$, but slightly above the values obtained from materials containing higher amounts of Co (Fig. 4i and S6). These values were consistent with those previously obtained from Ni-based chalcogenide.[18,53]

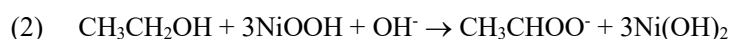
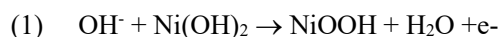
The proton diffusion is generally regarded as a rate-limiting step that controls the $\text{Ni}(\text{OH})_2 \rightleftharpoons \text{NiOOH}$

redox reaction in Ni-based electrodes.[54] In the scan rate range 60-100 mV s⁻¹ (Figure 4j), both the anodic and cathodic peak current (*i_p*) were found to be a linear function of the square root of scan rate (*v*^{1/2}), inferring a diffusion-limited redox reaction within the NiSe₂ and the bimetallic selenides. Thus, according to the Randles–Sevcik equation, we investigated the diffusion coefficient (*D*) of the redox limiting species within the electrodes using the following equation:[55]

$$I_p = 2.69 \times 10^5 n^{3/2} A D^{1/2} C v^{1/2}$$

where *n* and *C* are the electron transfer number (assumed to be 1) and the initial concentration of redox species, respectively. The concentration of Ni(II) was found to be 3.97 g cm⁻³, thus we estimated the *C* value to be 0.043 mol cm⁻³. [42,53] Based on this equation, the diffusion coefficient of the redox limiting species in the Ni_{0.75}Co_{0.25}Se₂ electrode was estimated at 1.2×10⁻⁹ cm² s⁻¹, an order of magnitude above that of the other two Ni-Co-based selenide electrodes (Fig. 4i and S6), but well below that of NiSe₂, 5.0×10⁻⁹ cm² s⁻¹.

The mechanism of the partial ethanol oxidation to acetate involves two main steps: (1) Ni(OH)₂ activated to NiOOH, and (2) the subsequent oxidation of the adsorbed intermediate:[56–59]



The Ni(OH)₂ oxidation to NiOOH is generally considered to be the limiting step.[60] The partial substitution of Ni by Co within the Ni₂Se certainly implies a slight reduction of the amount of surface NiOOH, but much higher EOR current densities were obtained for Ni_{0.75}Co_{0.25}Se₂ when compared with NiSe₂. This could be directly related to a higher surface area, better kinetics of NiOOH formation, and/or more effective ethanol adsorption by the introduction of Co in the NiSe₂ structure.[56]

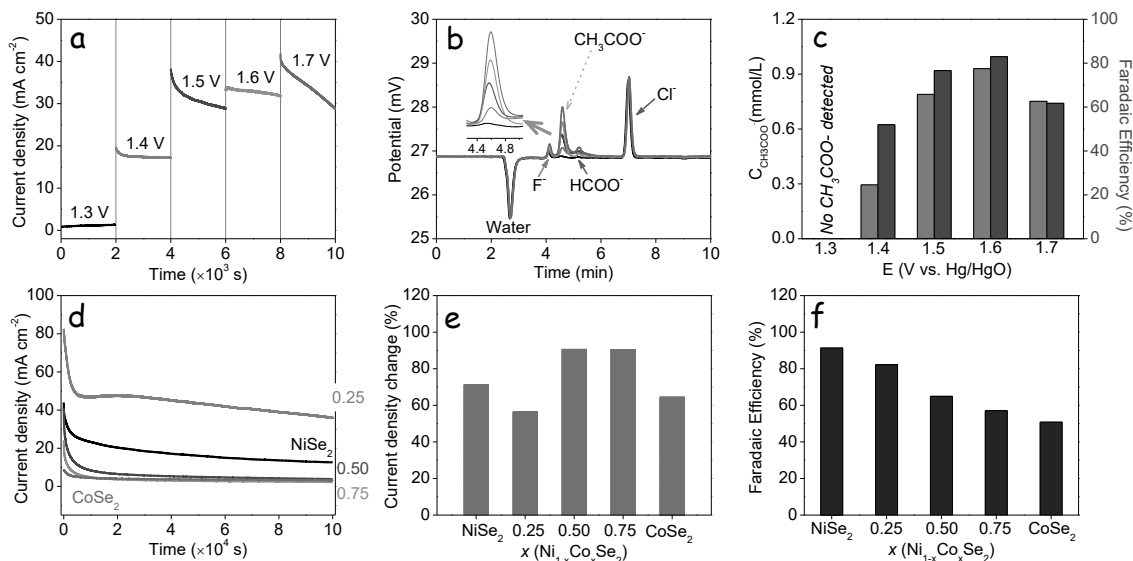


Fig. 5. Electrochemical performance of the bimetallic selenide electrode in 1M KOH + 1M ethanol. (a) CA curves of continuous 2,000 s operation for Ni_{0.75}Co_{0.25}Se₂ NPs at each potential of 1.3, 1.4, 1.5, 1.6, and 1.7 V. (b) IC profile at the end of each 2,000 s intervals. Inset shows the peaks at 4.6 min obtained at each potential. Black, red, blue, pink, and green curves were recorded at the 2000th, 4000th, 6000th, 8000th, and 10000th s respectively. (c) Calculated acetate concentration and Faradaic efficiency after 2,000 s testing at each potential for Ni_{0.75}Co_{0.25}Se₂. (d) CA curves for the selenide over the entire composition range at 1.50 V for 10,000 s testing. (e,f) Corresponding current density change and faradaic efficiency.

Fig. 5a displays the CA test for Ni_{0.75}Co_{0.25}Se₂ electrode in 1M KOH + 1M ethanol at 1.3, 1.4, 1.5, 1.6, and 1.7 V. After reacting for 2000 s, a small portion of the electrolyte was analyzed by IC (see details in the experimental section). As shown in Fig. 5b, the peak at 4.6 min in the IC profile was associated with acetate, which was the only identified product of the ethanol electrooxidation on Ni_{0.75}Co_{0.25}Se₂ electrodes. No acetate was detected at 1.3 V, where EOR was not activated on NiOOH. The cumulative acetate concentration in solution was quantified at 0.29, 1.08, 2.01, 2.77 mmol L⁻¹, corresponding to 9.2, 33.5, 61.1, and 82.6 μmol acetate produced at 1.4, 1.5, 1.6, and 1.7 V, respectively. If only considering the acetate production at each potential, the acetate concentration was found to be 0.29, 0.79, 0.93, and 0.75 mM, equaling to 9.2, 24.2, 27.7, and 21.4 μmol (Fig. 5c and Table S3). The acetate production increased with the applied potential, up to 1.6 V. Above this voltage,

competition with OER decreased the amount of acetate produced.

The Faradaic efficiency (FE) was calculated using the following equation:

$$FE(\%) = \frac{\text{mol of product} \times n \times F}{\text{total charge passed}} \times 100\%$$

where n is the electron transfer number (assumed to be 4 for the ethanol to acetate reaction), and F is the Faradaic constant (96485 C mol⁻¹).

For Ni_{0.75}Co_{0.25}Se₂ electrodes, the lowest Faradaic efficiency for the ethanol to acetate was achieved at 1.4 V, and it was found to increase above 80% at 1.6 V, and then decrease at higher potentials due to the activation of the competing OER. More quantitatively, a total charge of 6.9, 12.2, 12.9, and 13.4 C passed through the electrode at 1.4 V, 1.5 V, 1.6 V and 1.7 V, which translated into a Faradaic efficiency of 51.9%, 76.6%, 82.9% and 61.7%, respectively (Table S3).

The long-term stability of the electrocatalyst was tested using CA at 1.5 V. As can be seen in Fig. 5d, almost all the electrodes suffered a rapid decay in current density for the first several minutes. Around 71.3%, 56.4, 90.6%, 90.4, and 64.6% of the initial current densities were lost after 1x10⁴ s operation (Fig. 5e). The activity loss is mainly associated with the accumulation of strongly adsorbed intermediate species poisoning the active surface sites. But changes in the surface chemistry of the electrode, including element rearrangement, surface aggregation of the elements and phase evolution in alkaline media at a high external potential could also play an important role.[61–63]

For the Ni_{0.75}Co_{0.25}Se₂ electrode, a stable current density of 45 mA cm⁻², corresponding to 1.2 A g⁻¹, was sustained over the entire test after the initial rapid decay. IC analysis of the solution after 1x10⁴ s operation (Fig. S8) showed the produced acetate amount to reach 182.3 μmol for the Ni_{0.75}Co_{0.25}Se₂ electrode, well above the values obtained for NiSe₂ (80.2 μmol) and the other Ni-Co selenides (Table

S3). The rate of acetate production on the $\text{Ni}_{0.75}\text{Co}_{0.25}\text{Se}_2$ electrode was $0.34 \text{ mmol cm}^{-2} \text{ h}^{-1}$. In terms of Faradaic efficiency, NiSe_2 reached 91.3%, and this value decreased with the incorporation of Co (Table S4).

CA at 1.5 V in 1M KOH showed the contribution of current not associated to EOR to increase with the Co addition, from 1.9% for NiSe_2 and 1.8% for $\text{Ni}_{0.75}\text{Co}_{0.25}\text{Se}_2$, to values well above 10% for materials containing higher amounts of Co (Fig. S7b and Table S4). Thus the decrease of Faradaic efficiency with the increase of the Co content was associated with the enhanced OER performance.

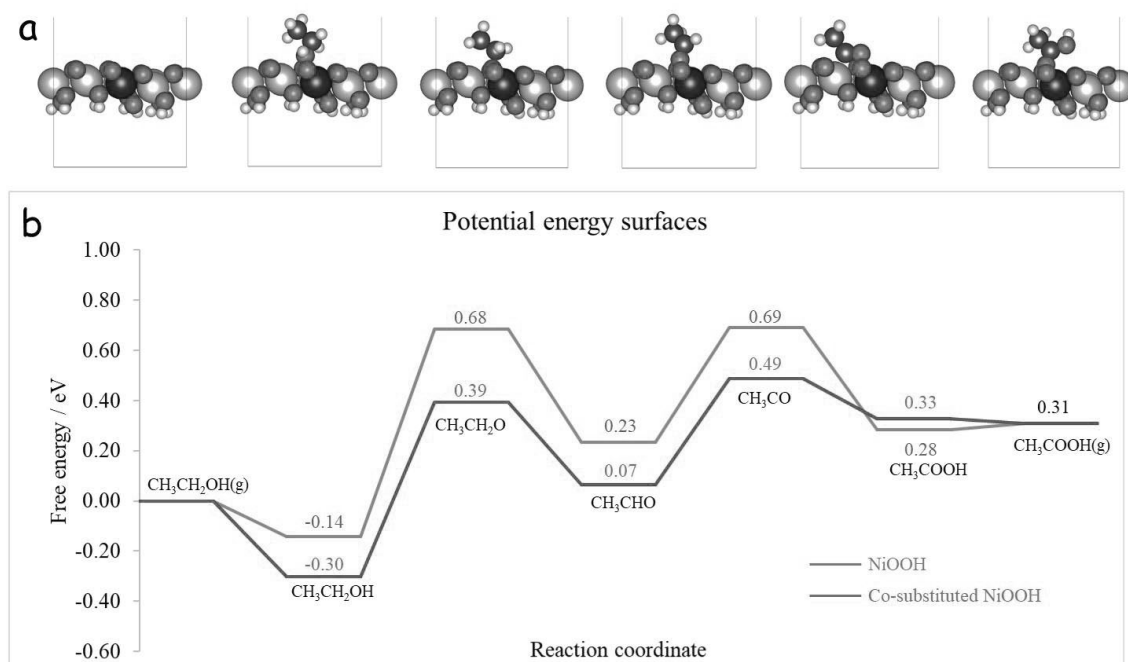


Fig. 6. (a) DFT optimized adsorbed intermediates on the Co-containing NiOOH surface of $\text{Ni}_{0.75}\text{Co}_{0.25}\text{Se}_2$ electrode, grey ball for Ni, blue for Co, red for O, orange for H, and wine for C. (b) Gibbs free energy diagrams for the ethanol conversion on NiOOH and Co-containing NiOOH surfaces.

The EOR electrocatalytic mechanism and the role of Co in the NiSe_2 electrode were systematically investigated by DFT. Since NiOOH is the active surface for EOR in alkaline solution, we built two slab models, NiOOH, and Co-substituted NiOOH. Fig. S9 and 6a show the adsorbed intermediates on

the NiOOH and Co-substituted NiOOH surface, respectively. Fig. 6b compares the corresponding Gibbs free energy diagram. The ethanol molecule adsorption energy was calculated to be -0.14 eV and -0.30 eV on the NiOOH and Co-substituted NiOOH surface, indicating stronger ethanol adsorption in the presence of cobalt. The presence of cobalt decreases the formation energy of the intermediate $\text{CH}_3\text{CH}_2\text{O}$ through a dehydrogenation process, from 0.82 eV for NiOOH, to 0.69 eV for Co-substituted NiOOH. The conversion of $\text{CH}_3\text{CH}_2\text{O}$ to CH_3CHO is energetically downwards for both catalysts, with a free energy change of -0.45 eV for and -0.32 eV for Co-substituted NiOOH. Both catalysts show a similar barrier (0.46 eV for NiOOH and 0.42 eV for Co-NiOOH) for the third dehydrogenation step, which results in adsorbed CH_3CO . This dehydrogenation process is generally accompanied by the reduction of NiOOH to $\text{Ni}(\text{OH})_2$. Last, adsorbed CH_3CO is released when interacting with OH^- ions to form CH_3COOH .

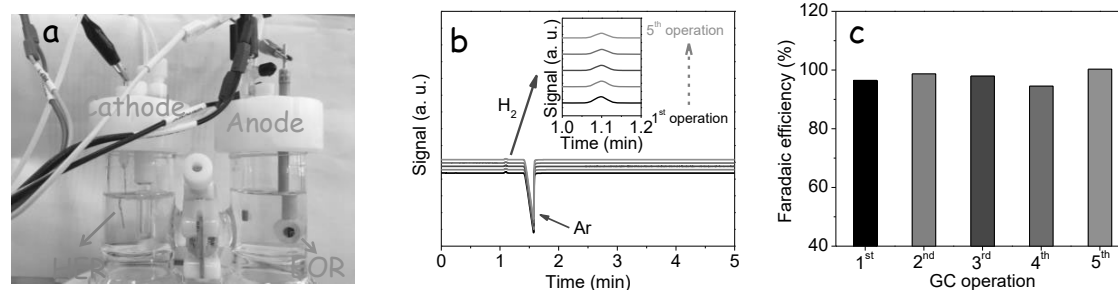


Fig. 7. (a) Setup for the H-type cell with two compartments. (b) GC curves within 1 hour GC sampling at the cathode. (c) Calculated Faradaic efficiency for HER.

To detect and quantify the gas product generated at the cathode, an H-type cell with two compartments separated by a proton exchange membrane was used (Fig. 7a). The cell contained 1 M KOH and 1 M ethanol in both compartments. At the cathode side, high-purity Ar was used to carry the produced gas to the GC. As can be seen in Fig. 7b, two peaks were located at ca. 1.1 and 1.5 min, which were associated to molecular hydrogen and argon. By comparing with known standard hydrogen

concentrations, the calculated Faradaic efficiency was determined to be nearly 100% (Fig. 7c), indicating that only hydrogen was produced on the cathode. In the absence and presence of ethanol in the electrolyte, a total charge of 1.6 C and 85.6 C passed through the $\text{Ni}_{0.75}\text{Co}_{0.25}\text{Se}_2$ electrode and the Pt wire, respectively (Table S4). In the presence of ethanol, over 50-fold higher hydrogen was produced during 10,000 s operation.

4. Conclusion

In summary, we developed a solution-based method to produce $\text{Ni}_{1-x}\text{Co}_x\text{Se}_2$ NPs with tuned metal ratios. The electrochemical performance of the materials was tested in 1 M KOH and 1 M KOH + 1 M ethanol aqueous electrolytes. CoSe_2 showed enhanced OER activity and NiSe_2 demonstrated a more efficient EOR. The incorporation of small amounts of Co to the NiSe_2 structure resulted in the highest EOR activities. DFT calculations showed that the presence of Co improved ethanol adsorption and decreased the barrier for ethanol dehydrogenation. A current density up to 82.3 mA cm^{-2} was achieved for $\text{Ni}_{0.75}\text{Co}_{0.25}\text{Se}_2$ in 1 M KOH + 1 M ethanol electrolyte at 1.55 V, which is twofold higher than that obtained for NiSe_2 . Over 10,000s testing, the optimized electrocatalyst delivered an average acetate production rate of $0.34 \text{ mmol cm}^{-2} \text{ h}^{-1}$. Additionally, the ethanol to acetate faradaic efficiency was determined as 82.3%. This work provides a cost-effective approach to the high Faradaic efficiency electrochemical reforming of ethanol with acetate co-production. This work is also an excellent example for other small molecules oxidation and conversion into valuable chemicals.

Acknowledgements

This work was supported by the UESTC start-up funding and the Recruitment Program of Thousand Youth Talents. It was also supported by the European Regional Development Funds and by the

Spanish Ministerio de Economía y Competitividad through the project SEHTOP (ENE2016-77798-C4-3-R) and NANOGEN (PID2020-116093RB-C43). X. Wang, C. Xing, X. Han, R. He, Z. Liang, and Y. Zhang are grateful for the scholarship from China Scholarship Council (CSC). X. Han and J. Arbiol acknowledge funding from Generalitat de Catalunya 2017 SGR 327. ICN2 acknowledges support from the Severo Ochoa Programme (MINECO, Grant no. SEV-2013-0295). IREC and ICN2 are funded by the CERCA Programme / Generalitat de Catalunya. Part of the present work has been performed in the framework of Universitat Autònoma de Barcelona Materials Science PhD program.

Conflict of interest

The authors declare no competing financial interest.

Reference

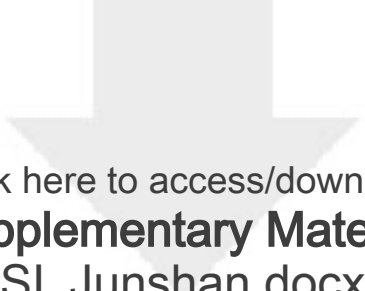
- [1] J.A. Turner, Sustainable hydrogen production, *Science* (80-.). 305 (2004) 972–974.
- [2] J.R. McKone, S.C. Marinescu, B.S. Brunschwig, J.R. Winkler, H.B. Gray, Earth-abundant hydrogen evolution electrocatalysts, *Chem. Sci.* 5 (2014) 865–878.
- [3] M. Besson, P. Gallezot, C. Pinel, Conversion of biomass into chemicals over metal catalysts, *Chem. Rev.* 114 (2014) 1827–1870.
- [4] B. You, Y. Sun, Innovative Strategies for Electrocatalytic Water Splitting, *Acc. Chem. Res.* 51 (2018) 1571–1580.
- [5] P.G. Levi, J.M. Cullen, Mapping Global Flows of Chemicals: From Fossil Fuel Feedstocks to Chemical Products, *Environ. Sci. Technol.* 52 (2018) 1725–1734.
- [6] V.G. Yadav, G.D. Yadav, S.C. Patankar, The production of fuels and chemicals in the new world: critical analysis of the choice between crude oil and biomass vis-à-vis sustainability and the environment, *Clean Technol. Environ. Policy.* 22 (2020) 1757–1774.
- [7] J. Garcia-Martinez, Chemistry 2030: A Roadmap for a New Decade, *Angew. Chemie - Int. Ed.* 60 (2021) 4956–4960.
- [8] L.T. Mika, E. Cséfalvay, Á. Németh, Catalytic Conversion of Carbohydrates to Initial Platform Chemicals: Chemistry and Sustainability, *Chem. Rev.* 118 (2018) 505–613.
- [9] Z. Zhang, G.W. Huber, Catalytic oxidation of carbohydrates into organic acids and furan chemicals, *Chem. Soc. Rev.* 47 (2018) 1351–1390.
- [10] B. Garlyyev, S. Xue, J. Fichtner, A.S. Bandarenka, C. Andronesco, Prospects of Value-Added Chemicals and Hydrogen via Electrolysis, *ChemSusChem.* 13 (2020) 2513–2521.
- [11] W.J. Liu, Z. Xu, D. Zhao, X.Q. Pan, H.C. Li, X. Hu, Z.Y. Fan, W.K. Wang, G.H. Zhao, S. Jin,

- G.W. Huber, H.Q. Yu, Efficient electrochemical production of glucaric acid and H₂ via glucose electrolysis, *Nat. Commun.* 11 (2020) 1–11.
- [12] L. Yaqoob, T. Noor, N. Iqbal, A comprehensive and critical review of the recent progress in electrocatalysts for the ethanol oxidation reaction, *RSC Adv.* 11 (2021) 16768–16804.
- [13] R.A. Dagle, A.D. Winkelman, K.K. Ramasamy, V. Lebarbier Dagle, R.S. Weber, Ethanol as a Renewable Building Block for Fuels and Chemicals, *Ind. Eng. Chem. Res.* 59 (2020) 4843–4853.
- [14] J. Dolfig, The microbial logic behind the prevalence of incomplete oxidation of organic compounds by acetogenic bacteria in methanogenic environments, *Microb. Ecol.* 41 (2001) 83–89.
- [15] B. You, X. Liu, X. Liu, Y. Sun, Efficient H₂ Evolution Coupled with Oxidative Refining of Alcohols via A Hierarchically Porous Nickel Bifunctional Electrocatalyst, *ACS Catal.* 7 (2017) 4564–4570.
- [16] Y. Tong, X. Yan, J. Liang, S.X. Dou, Metal-Based Electrocatalysts for Methanol Electro-Oxidation: Progress, Opportunities, and Challenges, *Small.* (2019) 1904126.
- [17] Y. Xu, M. Liu, S. Wang, K. Ren, M. Wang, Z. Wang, X. Li, L. Wang, H. Wang, Integrating Electrocatalytic Hydrogen Generation with Selective Oxidation of Glycerol to Formate over Bifunctional Nitrogen-Doped Carbon Coated Nickel-Molybdenum-Nitrogen Nanowire Arrays, *Appl. Catal. B Environ.* 298 (2021) 120493.
- [18] J. Li, C. Xing, Y. Zhang, T. Zhang, M.C. Spadaro, Q. Wu, Y. Yi, S. He, J. Llorca, J. Arbiol, A. Cabot, C. Cui, Nickel Iron Diselenide for Highly Efficient and Selective Electrocatalytic Conversion of Methanol to Formate, *Small.* 17 (2021) 2006623.
- [19] B. Zhao, J. Liu, C. Xu, R. Feng, P. Sui, L. Wang, J. Zhang, J.L. Luo, X.Z. Fu, Hollow NiSe Nanocrystals Heterogenized with Carbon Nanotubes for Efficient Electrocatalytic Methanol Upgrading to Boost Hydrogen Co-Production, *Adv. Funct. Mater.* 31 (2021) 2008812.
- [20] Q. Luo, M. Peng, X. Sun, A.M. Asiri, In situ growth of nickel selenide nanowire arrays on nickel foil for methanol electro-oxidation in alkaline media, *RSC Adv.* 5 (2015) 87051–87054.
- [21] B. Zhao, J. Liu, C. Xu, R. Feng, P. Sui, J.X. Luo, L. Wang, J. Zhang, J.L. Luo, X.Z. Fu, Interfacial engineering of Cu₂Se/Co₃Se₄ multivalent hetero-nanocrystals for energy-efficient electrocatalytic co-generation of value-added chemicals and hydrogen, *Appl. Catal. B Environ.* 285 (2021) 119800.
- [22] H. Mao, Z. Cao, X. Guo, M. Liu, D. Sun, Z. Sun, H. Ge, Y. Zhang, X.M. Song, Enhanced electrocatalytic performance for the oxidation of methanol by hierarchical NiS/Ni(OH)₂@polypyrrole/graphene oxide nanosheets, *Appl. Surf. Sci.* 471 (2019) 355–367.
- [23] Y. Yi, J. Li, C. Cui, Trimetallic FeCoNi disulfide nanosheets for CO₂-emission-free methanol conversion, *Chinese Chem. Lett.* (2021). <https://doi.org/10.1016/j.ccl.2021.07.005>
- [24] G. Kresse, J. Furthmüller, Efficiency of ab-initio total energy calculations for metals and semiconductors using a plane-wave basis set, *Comput. Mater. Sci.* 6 (1996) 15–50.
- [25] G. Kresse, J. Furthmüller, Efficient iterative schemes for ab initio total-energy calculations using a plane-wave basis set, *Phys. Rev. B - Condens. Matter Mater. Phys.* 54 (1996) 11169–11186.
- [26] J.P. Perdew, K. Burke, M. Ernzerhof, Generalized gradient approximation made simple, *Phys. Rev. Lett.* 77 (1996) 3865–3868.
- [27] D. Joubert, From ultrasoft pseudopotentials to the projector augmented-wave method, *Phys.*

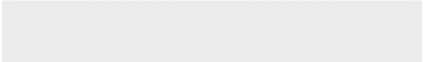

- Rev. B - Condens. Matter Mater. Phys. 59 (1999) 1758–1775.
- [28] P.E. Blöchl, Projector augmented-wave method, Phys. Rev. B. 50 (1994) 17953–17979.
- [29] S. Grimme, J. Antony, S. Ehrlich, H. Krieg, A consistent and accurate ab initio parametrization of density functional dispersion correction (DFT-D) for the 94 elements H-Pu, J. Chem. Phys. 132 (2010) 154104.
- [30] M. Castellanos, A.R. West, Deviations from Vegard's law in oxide solid solutions. The systems $\text{Li}_2\text{TiO}_3\text{-MgO}$ and $\text{Li}_2\text{TiO}_3\text{-Na}_2\text{TiO}_3$, J. Chem. Soc. Faraday Trans. 1 Phys. Chem. Condens. Phases. 76 (1980) 2159–2169.
- [31] Y. Zhang, C. Zhang, Y. Guo, D. Liu, Y. Yu, B. Zhang, Selenium vacancy-rich CoSe_2 ultrathin nanomeshes with abundant active sites for electrocatalytic oxygen evolution, J. Mater. Chem. A. 7 (2019) 2536–2540.
- [32] C. Zhang, J.J. Biendicho, T. Zhang, R. Du, J. Li, X. Yang, J. Arbiol, Y. Zhou, J.R. Morante, A. Cabot, Combined High Catalytic Activity and Efficient Polar Tubular Nanostructure in Urchin-Like Metallic NiCo_2Se_4 for High-Performance Lithium–Sulfur Batteries, Adv. Funct. Mater. 29 (2019) 1903842.
- [33] J.F. Moulder, W.F. Stickle, P.E. Sobol, K.D. Bomben, Handbook of X-ray photoelectron spectroscopy: a reference book of standard spectra for identification and interpretation of XPS data, Perkin- Elmer Corp., Minnesota, 1992. 84-85.
- [34] J.F. Moulder, W.F. Stickle, P.E. Sobol, K.D. Bomben, Handbook of X-ray photoelectron spectroscopy: a reference book of standard spectra for identification and interpretation of XPS data, 1992. 82-83.
- [35] J.F. Moulder, W.F. Stickle, P.E. Sobol, K.D. Bomben, Handbook of X-ray photoelectron spectroscopy: a reference book of standard spectra for identification and interpretation of XPS data, Minnesota, 1992. 96-97.
- [36] L. Nguyen, F.F. Tao, Y. Tang, J. Dou, X.J. Bao, Understanding Catalyst Surfaces during Catalysis through Near Ambient Pressure X-ray Photoelectron Spectroscopy, Chem. Rev. 119 (2019) 6822–6905.
- [37] D.M. MacArthur, The Hydrated Nickel Hydroxide Electrode Potential Sweep Experiments, The Electrochemical Society, 1970.117.4.
- [38] J. Li, Z. Luo, F. He, Y. Zuo, C. Zhang, J. Liu, R. Du, X. Yu, T. Zhang, P. Tang, M.F.I. Carrió, J. Arbiol, J. Llorca, A. Cabot, Colloidal Ni-Co-Sn Nanoparticles as Efficient Electrocatalysts for the Methanol Oxidation Reaction, J. Mater. Chem. A. 6 (2018) 22915–22924.
- [39] X. Cui, W. Guo, M. Zhou, Y. Yang, Y. Li, P. Xiao, Y. Zhang, X. Zhang, Promoting effect of Co in Ni_mCo_n (m + n = 4) bimetallic electrocatalysts for methanol oxidation reaction, ACS Appl. Mater. Interfaces. 7 (2015) 493–503.
- [40] S. Rezaee, S. Shahrokhian, Facile synthesis of petal-like NiCo/NiO-CoO/nanoporous carbon composite based on mixed-metallic MOFs and their application for electrocatalytic oxidation of methanol, Appl. Catal. B Environ. 244 (2019) 802–813.
- [41] D. Wu, W. Zhang, D. Cheng, Facile Synthesis of Cu/NiCu Electrocatalysts Integrating Alloy, Core–Shell, and One-Dimensional Structures for Efficient Methanol Oxidation Reaction, ACS Appl. Mater. Interfaces. 9 (2017) 19843–19851.
- [42] J. Li, Z. Luo, Y. Zuo, J. Liu, T. Zhang, P. Tang, J. Arbiol, J. Llorca, A. Cabot, NiSn bimetallic nanoparticles as stable electrocatalysts for methanol oxidation reaction, Appl. Catal. B Environ. 234 (2018) 10–18.

- [43] J. Li, Y. Zuo, J. Liu, X. Wang, X. Yu, R. Du, T. Zhang, M.F. Infante-Carrió, P. Tang, J. Arbiol, J. Llorca, Z. Luo, A. Cabot, Superior methanol electrooxidation performance of (110)-faceted nickel polyhedral nanocrystals, *J. Mater. Chem. A*. 7 (2019) 22036–22043.
- [44] A. Cuña, C. Reyes Plascencia, E.L. da Silva, J. Marcuzzo, S. Khan, N. Tancredi, M.R. Baldan, C. de Fraga Malfatti, Electrochemical and spectroelectrochemical analyses of hydrothermal carbon supported nickel electrocatalyst for ethanol electro-oxidation in alkaline medium, *Appl. Catal. B Environ.* 202 (2017) 95–103.
- [45] L. Dai, Q. Qin, X. Zhao, C. Xu, C. Hu, S. Mo, Y.O. Wang, S. Lin, Z. Tang, N. Zheng, Electrochemical partial reforming of ethanol into ethyl acetate using ultrathin Co₃O₄ nanosheets as a highly selective anode catalyst, *ACS Cent. Sci.* 2 (2016) 538–544.
- [46] W. Wang, Y.B. Zhu, Q. Wen, Y. Wang, J. Xia, C. Li, M.W. Chen, Y. Liu, H. Li, H.A. Wu, T. Zhai, Modulation of Molecular Spatial Distribution and Chemisorption with Perforated Nanosheets for Ethanol Electro-oxidation, *Adv. Mater.* 31 (2019) 1900528.
- [47] G.F. Chen, Y. Luo, L.X. Ding, H. Wang, Low-Voltage Electrolytic Hydrogen Production Derived from Efficient Water and Ethanol Oxidation on Fluorine-Modified FeOOH Anode, *ACS Catal.* 8 (2018) 526–530.
- [48] S. Sheng, K. Ye, L. Sha, K. Zhu, Y. Gao, J. Yan, G. Wang, D. Cao, Rational design of Co-S-P nanosheet arrays as bifunctional electrocatalysts for both ethanol oxidation reaction and hydrogen evolution reaction, *Inorg. Chem. Front.* 7 (2020) 4498–4506.
- [49] S. Sheng, Y. Song, L. Sha, K. Ye, K. Zhu, Y. Gao, J. Yan, G. Wang, D. Cao, Simultaneous hydrogen evolution and ethanol oxidation in alkaline medium via a self-supported bifunctional electrocatalyst of Ni-Fe phosphide/Ni foam, *Appl. Surf. Sci.* 561 (2021) 150080.
- [50] Y. Ding, Q. Xue, Q.L. Hong, F.M. Li, Y.C. Jiang, S.N. Li, Y. Chen, Hydrogen and Potassium Acetate Co-Production from Electrochemical Reforming of Ethanol at Ultrathin Cobalt Sulfide Nanosheets on Nickel Foam, *ACS Appl. Mater. Interfaces.* 13 (2021) 4026–4033.
- [51] C.C.L. McCrory, S. Jung, J.C. Peters, T.F. Jaramillo, Benchmarking Heterogeneous Electrocatalysts for the Oxygen Evolution Reaction, *J. Am. Chem. Soc.* 135 (2013) 16977–16987.
- [52] D. Chen, S.D. Minteer, Mechanistic study of nickel based catalysts for oxygen evolution and methanol oxidation in alkaline medium, *J. Power Sources.* 284 (2015) 27–37.
- [53] X. Cui, P. Xiao, J. Wang, M. Zhou, W. Guo, Y. Yang, Y. He, Z. Wang, Y. Yang, Y. Zhang, Z. Lin, Highly Branched Metal Alloy Networks with Superior Activities for the Methanol Oxidation Reaction, *Angew. Chemie - Int. Ed.* 56 (2017) 4488–4493.
- [54] L. Xiao, J.T. Lu, P.F. Liu, L. Zhuang, J. Yan, Y. Hu, B. Mao, C. Lin, Proton diffusion determination and dual structure model for nickel hydroxide based on potential step measurements on single spherical beads, *J. Phys. Chem. B.* 109 (2005) 3860–3867.
- [55] A.J. Bard, L.R. Faulkner, N. York, C. @bullet, W. Brisbane, S.E. Toronto, Electrochemical methods: fundamentals and applications, 2nd editio, John Wiley & Sons, Inc., New York, Chichester, Weinheim, Brisbane, Singapore, Toronto, 2001.
- [56] A. Kowal, S.N. Port, R.J. Nichols, Nickel hydroxide electrocatalysts for alcohol oxidation reactions: An evaluation by infrared spectroscopy and electrochemical methods, *Catal. Today.* 38 (1997) 483–492.
- [57] M. Fleischmann, K. Korinek, D. Pletcher, The oxidation of organic compounds at a nickel anode in alkaline solution, *J. Electroanal. Chem.* 31 (1971) 39–49.

- [58] M. Fleischmann, K. Korinek, D. Pletcher, The kinetics and mechanism of the oxidation of amines and alcohols at oxide-covered nickel, silver, copper, and cobalt electrodes, *J. Chem. Soc. Perkin Trans. 2.* (1972) 1396–1403.
- [59] M.T. Bender, Y.C. Lam, S. Hammes-Schiffer, K.S. Choi, Unraveling Two Pathways for Electrochemical Alcohol and Aldehyde Oxidation on NiOOH, *J. Am. Chem. Soc.* 142 (2021) 21538–21547.
- [60] M.A.A. Rahim, R.M.A. Hameed, M.W. Khalil, Nickel as a catalyst for the electro-oxidation of methanol in alkaline medium, *J. Power Sources.* 134 (2004) 160–169.
- [61] A.A. Dubale, Y. Zheng, H. Wang, R. Hübner, Y. Li, J. Yang, J. Zhang, N.K. Sethi, L. He, Z. Zheng, W. Liu, High-Performance Bismuth-Doped Nickel Aerogel Electrocatalyst for the Methanol Oxidation Reaction, *Angew. Chemie - Int. Ed.* 59 (2020) 13891–13899.
- [62] X. Yu, Z. Luo, T. Zhang, P. Tang, J. Li, X. Wang, J. Llorca, J. Arbiol, J. Liu, A. Cabot, Stability of Pd₃Pb Nanocubes during Electrocatalytic Ethanol Oxidation, *Chem. Mater.* 32 (2020) 2044–2052.
- [63] Y. Zuo, Y. Liu, J. Li, R. Du, X. Han, T. Zhang, J. Arbiol, N.J. Divins, J. Llorca, N. Guijarro, K. Sivula, A. Cabot, In Situ Electrochemical Oxidation of Cu₂S into CuO Nanowires as a Durable and Efficient Electrocatalyst for Oxygen Evolution Reaction, *Chem. Mater.* 31 (2019) 7732–7743.



Click here to access/download
Supplementary Material
SI_Junshan.docx





Advanced Materials Research Area

Functional Nanomaterials Group

Jardi de les Dones de Negre 1
08930, Sant Adria del Besos, Barcelona (Spain)
Tel. +34 93 403 9154
Fax +34 93 402 11 48

Chemical Engineering Journal

Dec 16th, 2021

To whom this may concern:

The authors declare that they have no known competing financial interests or personal relationships that could have appeared to influence the work reported in this paper.

Thank you for your consideration of our potential contribution.

Sincerely,

A handwritten signature in black ink, appearing to read 'Andreu Cabot', is written over a large, stylized circular flourish.

Prof. Andreu Cabot
Advanced Material Research Department
Catalonia Institute for Energy Research - IREC
Phone: +34 625615115
E-mail: acabot@irec.cat